CHAPTER IV
RESULTS AND DISCUSSION

Chapter IV discusses and analyzes the experimental results, including computer simulations of the ion source, octupole deflector, Einzel lens, and the fully integrated system. It also presents the assembly of the compact beamline system, which includes the vacuum components and the power supplies mounted beneath the beamline. Finally, the chapter explains the results from the vacuum heater coil tests conducted on the ionizer.

4.1 Computer simulation results

In both the simulation and the system assembly, the distances follow the optical layout as shown in Figure 4.1.

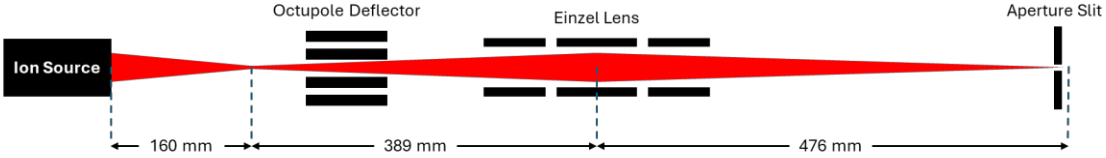

Figure 4.1 Optical layout of the negative carbon ion beamline.

In the simulations, a mesh convergence study is always performed before finalizing the results of each model. For example, a convergence study was conducted on the ion source model, as shown in Figure 4.2, to determine the optimal cell size. This ensures accurate results while conserving computational resources and reducing simulation time.

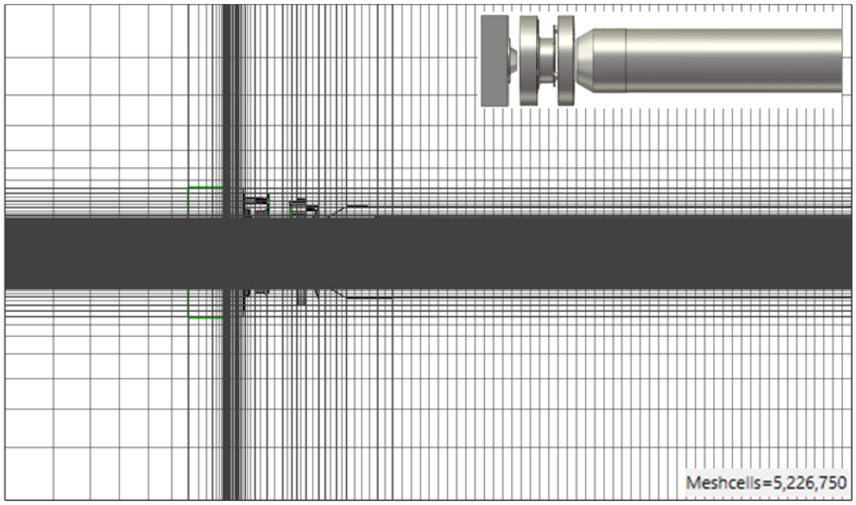

Figure 4.2 Optimal mesh size of the ion source model.

4.1.1 Convergence study

The parameter *N_mesh* was varied to increase mesh density in regions near surfaces or areas requiring high detail. *N_mesh* represents the number of cells per maximum model box edge. A parameter sweep was performed across ten values of *N_mesh* (ranging from 20 to 200). The results showed that increasing the mesh density beyond *N_mesh* = 20 led to changes of less than 1%, meeting the commonly accepted convergence threshold of approximately 1% used in Field/PIC/FEM studies. This threshold balances the need for high accuracy with acceptable computational cost.

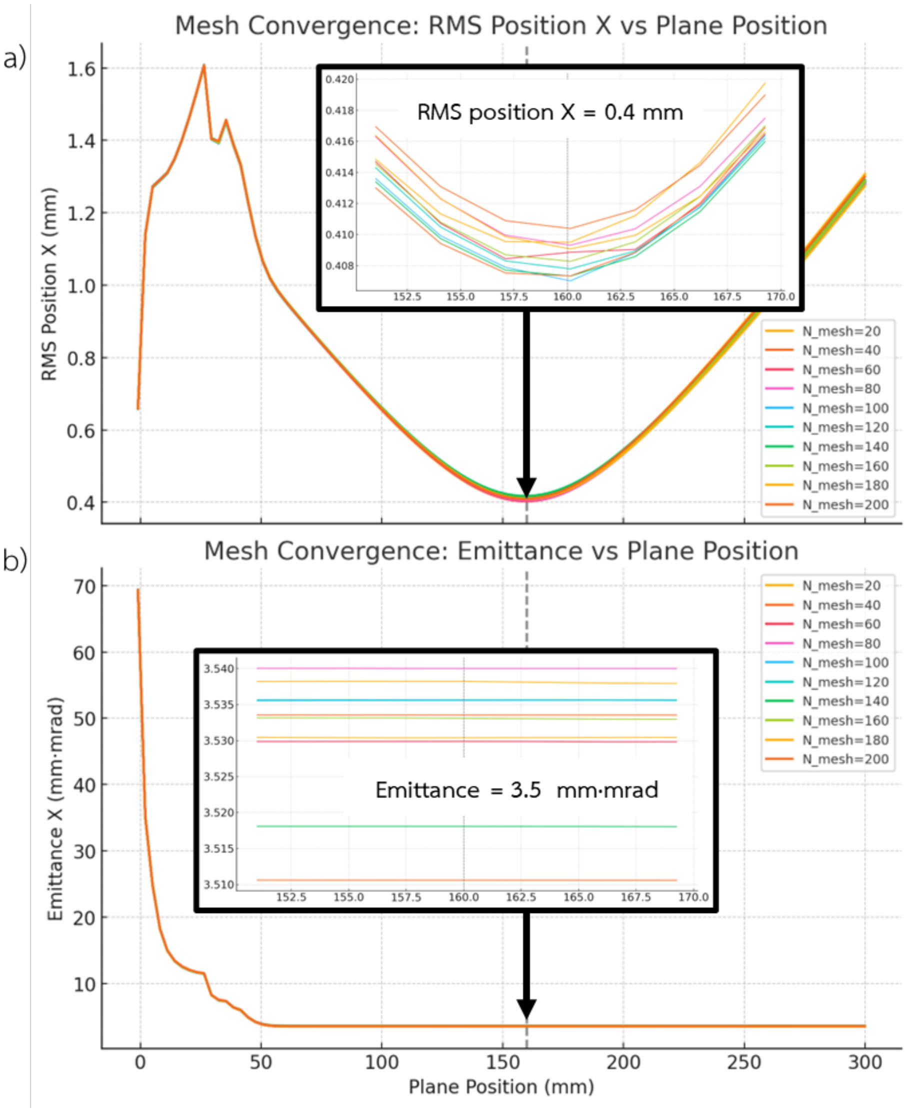

Figure 4.3 Convergence study graphs used to select the optimal mesh size for the ion source model. a) rms(position_x) vs. plane position b) Emittance vs. plane position.

From Figure 4.3, it is observed that the results converge when considering both the *rms(position_x)* and emittance on the particle monitor along the beam path. The ion source's focal point is located 160 mm from the sample target, where the *rms(position_x)* is 0.4 mm—consistent with the beam image in Figure 3.7b—and the emittance stabilizes at 3.5 mm·mrad immediately after extraction. Based on these findings, a mesh density corresponding to *N_mesh* = 20—the lowest value tested—was selected. This choice results in a total of 5,226,750 cells for the ion source model simulation, as shown in Figure 4.2.

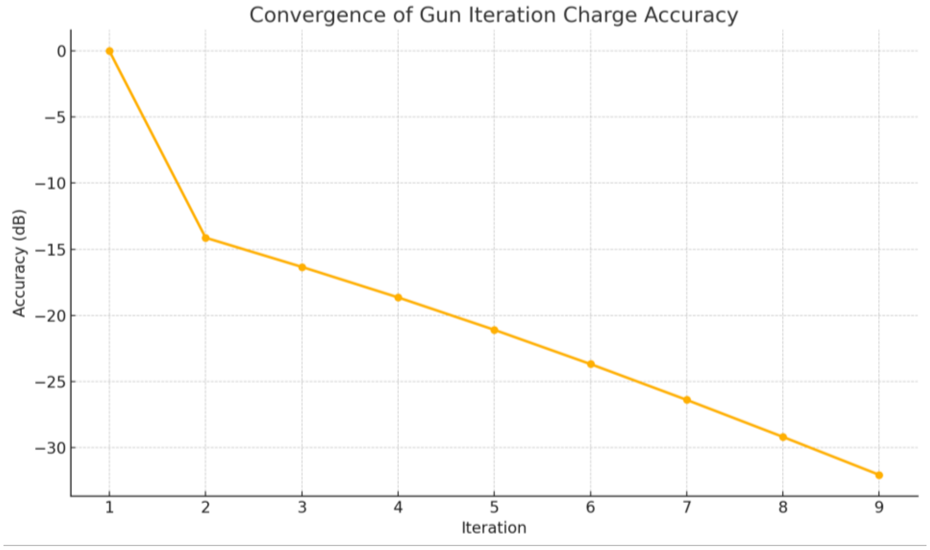

Figure 4.4 Convergence of gun iteration vs. charge accuracy.

4.1.2 The study of miss alignment of the octupole deflector

Based on the available alignment tools and system design, engineers defined the maximum possible alignment errors as a 1 mm offset and a 2° tilt. In the simulation, two parameters were varied: the tilt angle (θ) at 0°, 0.5°, 1°, 1.5°, and 2°, and the octupole deflector's y-axis offset at 0, 0.5, 1, 1.5, and 2 mm. The objective was to determine whether the beam, under worst-case misalignment conditions, still focuses onto and passes through the aperture slit. Beam acceptance was evaluated by analyzing the particle monitor images at the slit, which has a maximum opening of 20 × 20 mm².

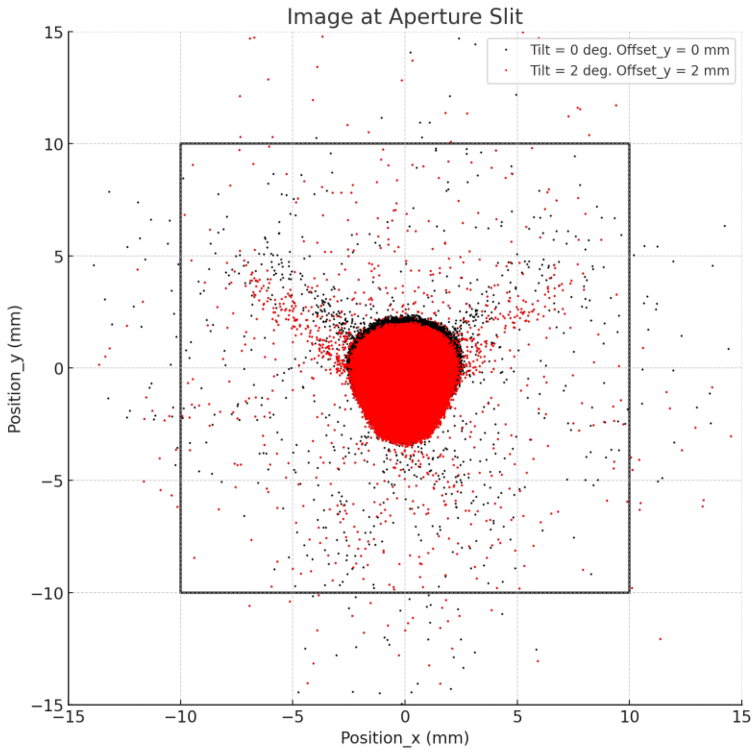

Figure 4.5 Comparison of particle images at the aperture slit between perfect alignment (black) and tilt = 2° with offset = 2 mm (red). The black square indicates the maximum slit opening of 20 × 20 mm^2.

The simulations demonstrated that in all 25 misalignment scenarios, over 99% of the ions successfully passed through the fully open 20 × 20 mm^2 slit and remained focused. Two representative cases are compared in Figure 4.3: perfect alignment ($\theta = 0°$, offset = 0 mm) and the worst-case misalignment ($\theta = 2°$, offset = 2 mm). In the worst-case scenario, the ion beam was displaced by 1 mm along the y-axis at the focal plane, as shown in the histogram in Figure 4.6, while the overall beam shape remained essentially unchanged. This displacement can be corrected by increasing the electric field through the application of a bias voltage to the octupole rod on the side toward which the beam has shifted. Chomchan et al. (2024) demonstrated (Figure 2.6) that applying up to 300 V to a single octupole rod can steer the beam by approximately 1.5 mm downstream of the deflector. Therefore, the octupole deflector—with its independent x–y steering capability—can reliably compensate for misalignment errors.

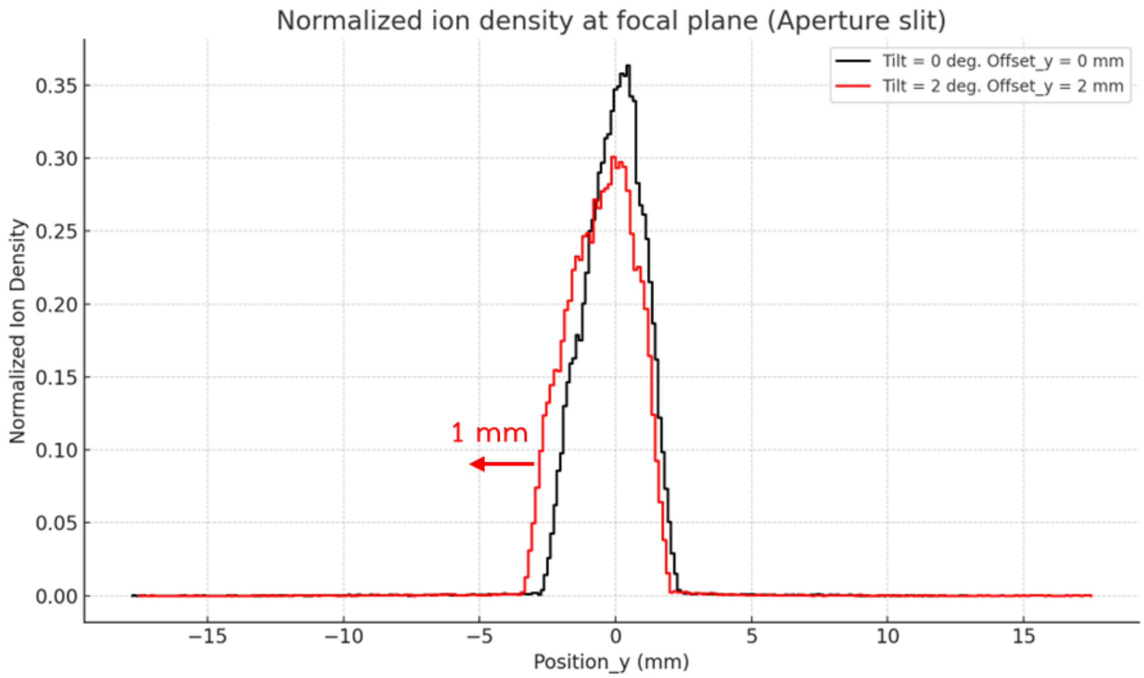

Figure 4.6 Comparison of normalized ion density at the aperture slit for perfect alignment (black) and for the worst-case misalignment with θ = 2° and offset = 2 mm (red), shown as a histogram.

4.1.3 Einzel lens simulation results

4.1.3.1 The study of effects from mounting support

The first model, including its mounting supports shown in Figure 4.7a, produced a three-lobed beam profile at the focal plane downstream of the Einzel lens. This distortion was caused by electric-field perturbations (Figure 4.8) from the three long stainless-steel support rods on rings 1 and 3. To correct this, the model was revised as shown in Figure 4.7b by reducing the gap between the support rings and adopting the dimensions from Suethonglang et al. (2024).

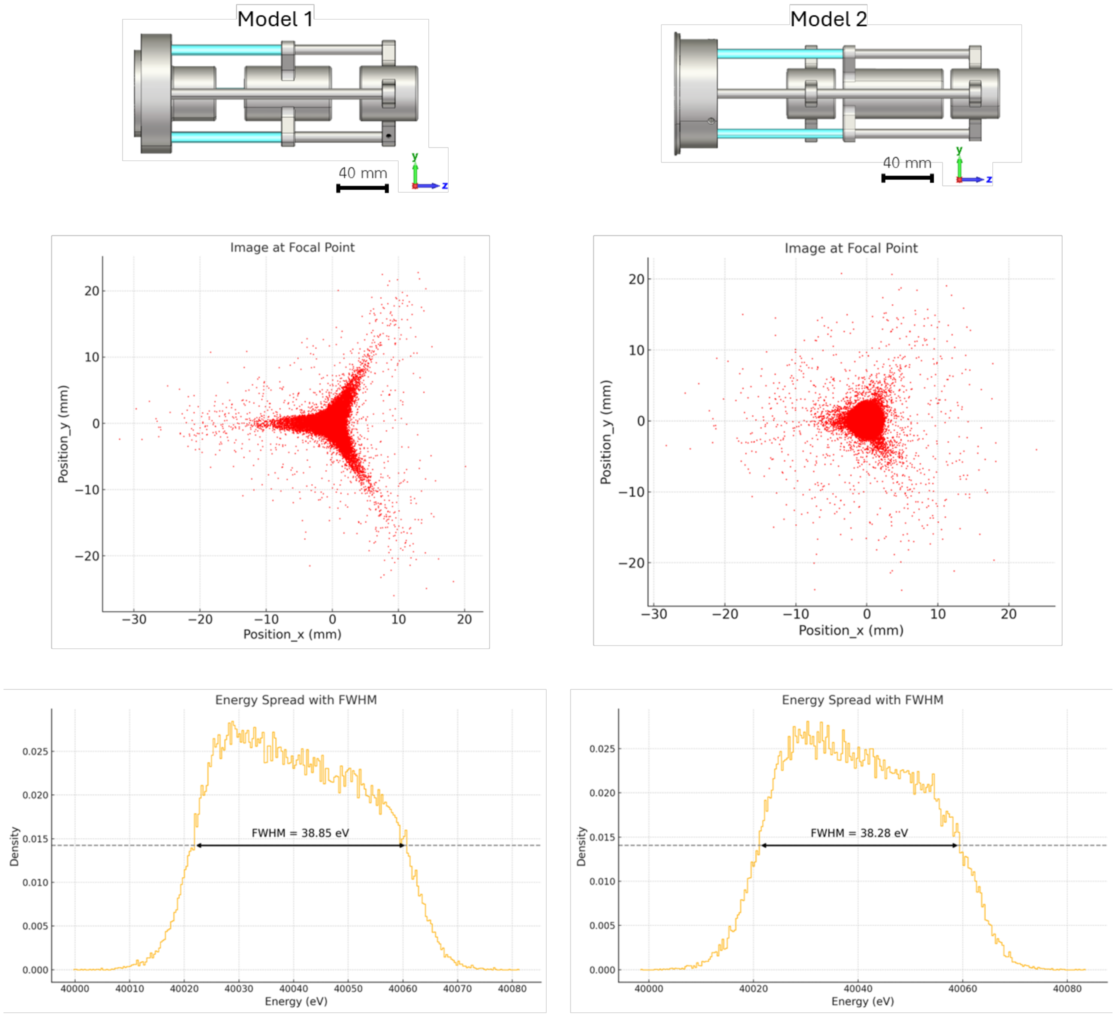

a) b)

Figure 4.7 Simulated beam image at the focal plane using a −20 kV bias on the central electrode. a) Model 1 with ratio of 43 : 21 : 64 mm. b) Model 2 ratio of 40 : 6 : 82 mm. The insulator segment is shown in blue.

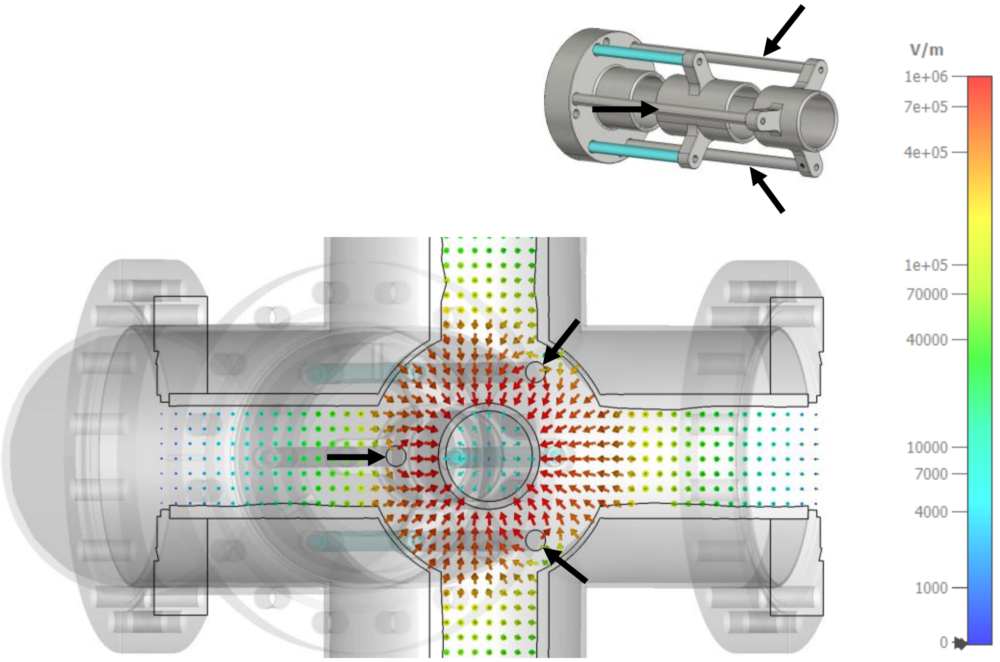

Figure 4.8 The electric field inside Einzel lens model 1 is shown in a cross-sectional view to illustrate the electric field perturbations around the support rods (black arrows).

After updating to Model 2, the beam image still exhibits slight lobes. This distortion is unavoidable, as the electric field from the support rods penetrates the ion beam path. To minimize this effect, the gap between the support rings was reduced to 6 mm—the minimum allowable distance without risking electrical breakdown. In ultra-high vacuum conditions (10^{-6} to 10^{-9} Torr), the dielectric strength typically ranges from 20 to 40 MV/m (20–40 kV/mm); however, practical values between 5 and 20 kV/mm have been reported by Ratkus et al. (2024), depending on electrode surface finish and geometry.

Moreover, the Model 2 design focuses the ion beam more effectively than Model 1, as shown in Figure 4.9. When the same –20 kV bias is applied to the Einzel lens, Model 2 achieves a focal distance of 900 mm from the source, compared to 1100 mm for Model 1. The shorter focal length reduces the power required from the supply, making Model 2 more energy-efficient. Based on these advantages, Model 2 was selected for use in the negative carbon ion beamline in AMS.

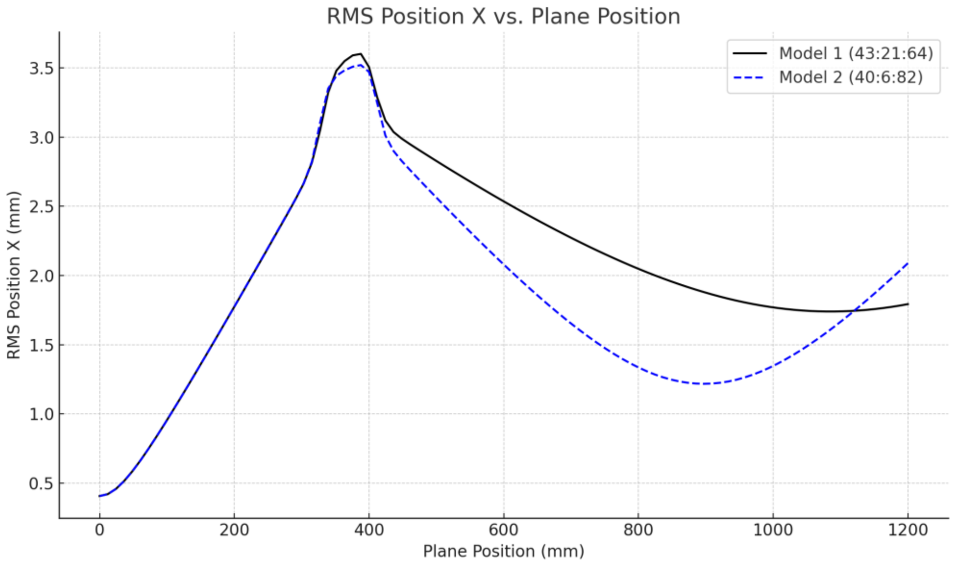

Figure 4.9 Comparison of the focal distances of Einzel lens Model 1 and Model 2.

4.1.3.2 The study of focal range

Using Einzel lens Model 2, which has dimensions of 40 : 6 : 82 mm, further studies were conducted with the selected negative-polarity power supply from Matsusada Precision, Inc., capable of delivering up to 30 kV. Bias voltages ranging from 0 V to –30 kV were applied to the central electrode in ten increments (0 V, –2.5 kV, –5 kV, ..., –30 kV), as shown in Figure 4.10. These simulations enabled the examination of the corresponding focal distances at each voltage level.

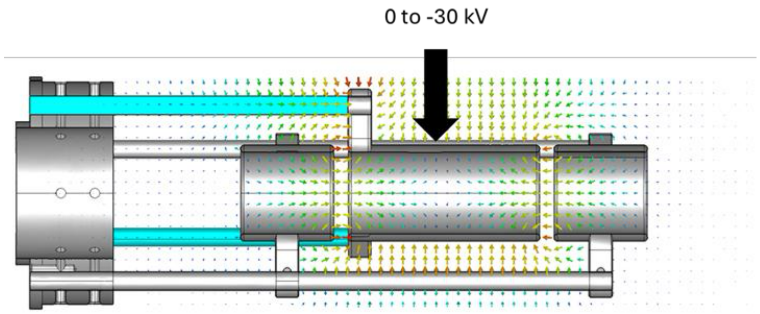

Figure 4.10 Cross-sectional view of the electric field within the Einzel lens, showing how the field strength varies with the applied bias voltage.

The results showed that increasing the central-electrode voltage strengthened the electric field and shortened the focal length, reaching a minimum of 83.61 mm downstream from the lens center at –30 kV. At –17.5 kV, the ion beam was nearly parallel.

A shorter focal length requires a stronger field, which pulls the beam into a tighter convergence and produces a larger convergence angle. After the focus, that same angle causes rapid divergence. In other words, a short focal length yields a smaller spot size at the focus but increases aberrations and space-charge effects, causing the beam to spread out more quickly beyond the focal point as shown in Figure 4.12.

The optimizer function was then used to determine the ideal bias voltage needed to focus the ion beam at 865 mm—the position of the aperture slit measured from the source. The study found that a voltage of −20,139 V was required, which falls within the operating range of the power supply selected for the AMS radiocarbon dating system.

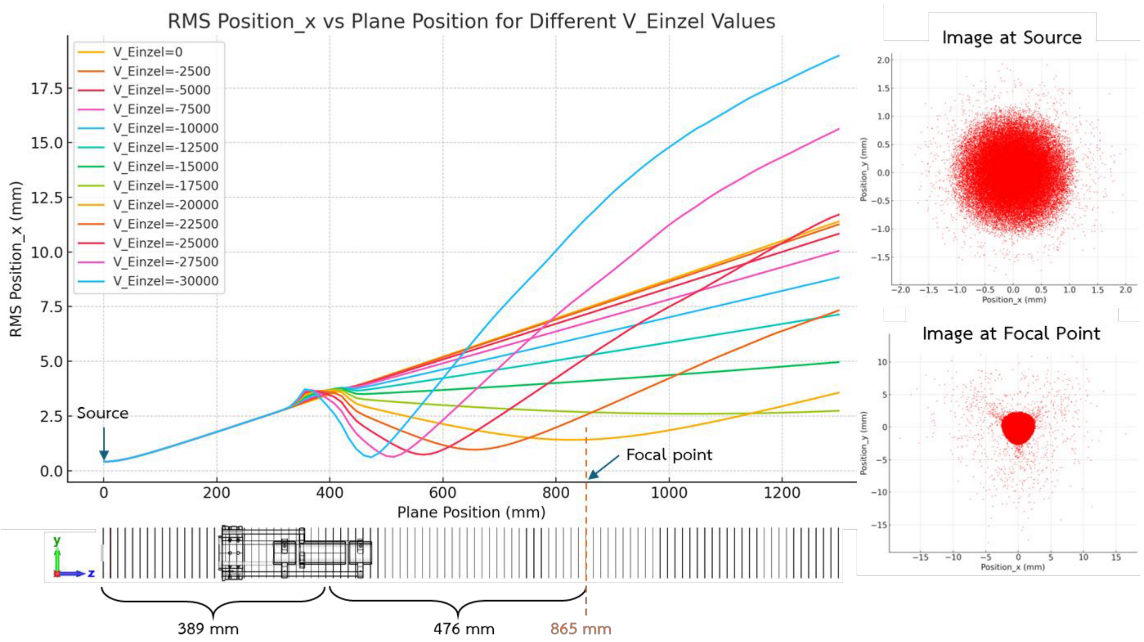

Figure 4.11 Graph showing the relationship between plane position and *rms(position_x)* for various *V_Einzel* values. The plot also indicates the distance from the source to the center of the Einzel lens (389 mm) and the distance from the lens center to the aperture slit (476 mm).

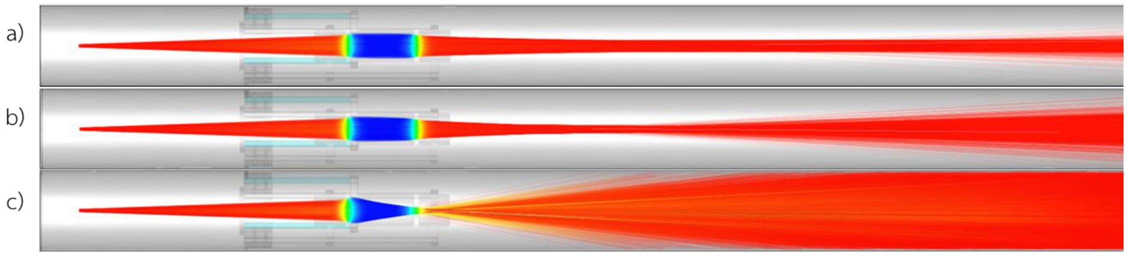

Figure 4.12 Trajectories of negative carbon ions through the Einzel lens. a) −17.5 kV, producing an almost parallel beam. b) −20,139 V (from the optimizer), focused exactly at the aperture slit. c) −30 kV, the maximum output of the power supply.

4.1.3.3 The study of miss alignment

In this section, the practical challenges of assembling the Einzel lens downstream of the octupole deflector are addressed. Both components share common mounting supports on a CF152 vacuum chamber flange. Acknowledging that perfect alignment is unattainable in the actual system, maximum assembly errors were defined as a 1 mm offset and a 2° tilt, based on the limitations of the available tooling.

With the central electrode biased at −17,500 V, a total of 81 misalignment scenarios were investigated. In the worst-case scenario—featuring a 1.6 mm offset and a 1.6° tilt—the ion beam trajectory deviated significantly from the optical axis and struck the chamber wall, as shown in Figure 4.13. This led to complete beam loss, with no beam focusing observed at the aperture slit.

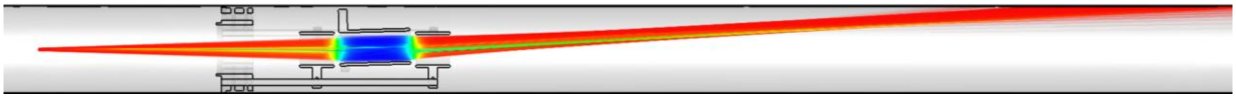

Figure 4.13 Trajectories of C^{-} ions through the Einzel lens with a middle electrode 1.6° tilt and 1.6 mm offset from the optical axis.

The results from the particle monitor at the aperture slit, evaluating whether the beam remained focused on and passed through the slit under varied parameters, are presented in Table 4.1.

Table 4.1 Acceptable tolerances for the central electrode of the Einzel Lens.

Offset_y (mm)	Tilt angle (θ)
0.0	0.6
0.2	0.4
0.4	0.2

The table shows that the middle electrode cannot be offset by more than 0.4 mm, nor tilted by more than 0.6°, with other tolerances kept at zero. This differs from the octupole deflector, which maintained beam focus at the slit even with a 2° tilt and 2 mm offset. The stricter tolerances for the Einzel lens result from the very strong electric field between the central and side electrodes. Even a slight misalignment breaks the field symmetry and immediately deflects the ion beam.

4.1.4 Low-energy negative carbon ion beamline simulation results

In this section, the results of the end-to-end beamline simulation are presented, encompassing the ion source, octupole deflector, Einzel lens, and aperture slit within a fully integrated CST model. To streamline the simulation, nonessential hardware—such as vacuum pumps, chamber fittings, and screws—was omitted. The particle distribution at the ion source focus was imported using the Particle Import Interface. Under ideal, perfectly aligned conditions, the optimized bias voltage of –20,139 V was applied to the Einzel lens. The beam size, emittance, beam envelope, and particle image were then tracked along the optical axis using a 2D monitor placed at the aperture slit and a series of 100 monitors positioned from the source focus to just beyond the slit.

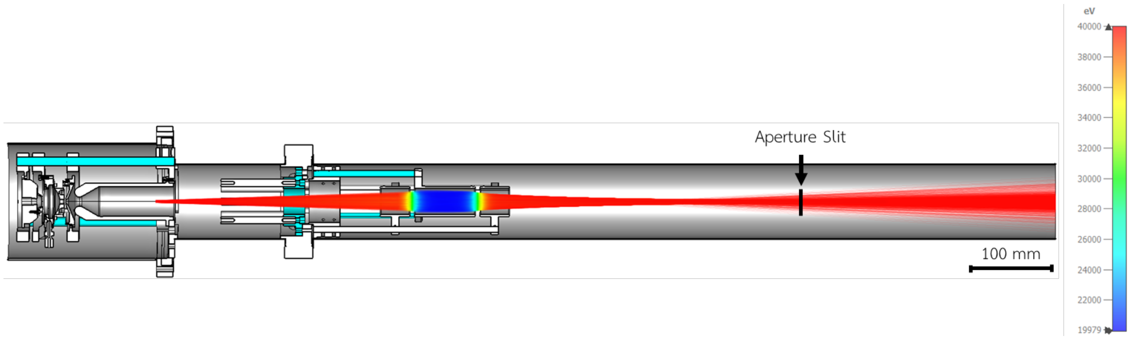

Figure 4.14 Trajectories of C^{-} ions passing through the perfectly aligned low-energy negative carbon ion beamline.

At the aperture slit, the ion beam emittance was found to be 8 mm·mrad at 40 keV. When multiplied by the square root of the beam energy in MeV (√0.04 MeV), this yields 1.6 mm·mrad·√MeV—well within the design requirement of keeping the emittance below 10 π·mm·mrad·√MeV at the slit. This confirms the system's ability to deliver a negative carbon ion beam up to 40 keV with adjustable focal length and independent X–Y steering. The beam size, based on *rms(position_x)* and *rms(position_y)*, was approximately 2.42 × 2.38 mm² (Figure 4.15). Furthermore, 99% of the ions successfully passed through the fully open slit.

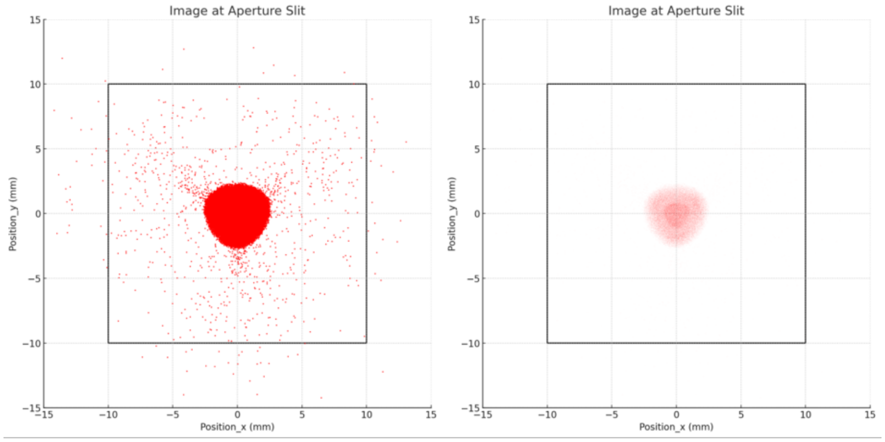

a)

b)

Figure 4.15 Particle images at the aperture slit for the perfectly aligned low energy negative carbon ion beamline. The black square indicates the maximum slit opening of 20 × 20 mm². Figure a) mark size = 1.5 and Figure b) mark size = 0.1

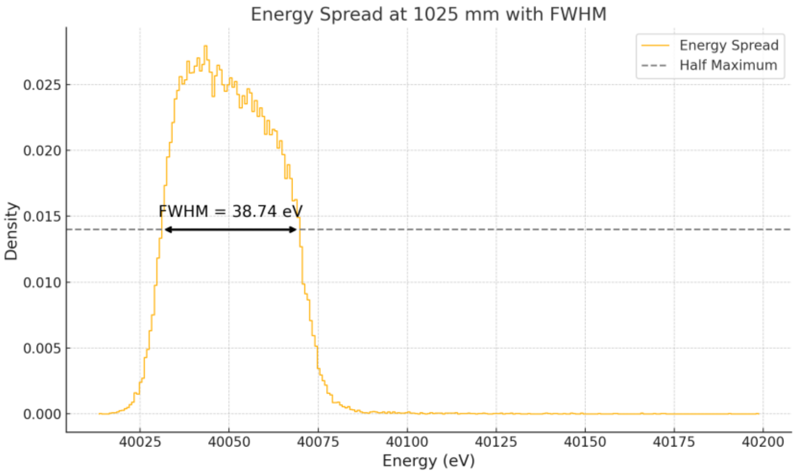

Figure 4.16 Energy spread with FWHM at the aperture slit location.

4.2 Low-energy beamline design

4.2.1 Leak checking by helium detector

Figure 4.17 Digital display of the helium leak rate during vacuum component testing.

By selecting existing vacuum components from SLRI, each part was first cleaned with alcohol to remove contaminants. A leak check was then performed using a Pfeiffer Adixen ASM 340 leak detector. All components were found to be suitable for use, with measured helium leak rates on the order of 10^{-9} mbar·L/s—well below the 10^{-8} mbar·L/s threshold—indicating that the chambers were leak-tight and ready for operation. These components were therefore selected for assembly in the AMS beamline.

4.2.2 High voltage power supply

A suitable high-voltage power supply configuration for the low-energy negative carbon ion beamline was selected from Matsusada Precision, Inc. The system uses 10 DC power supplies, all powered from a 220 V AC input. For the cesium-sputter ion source, five HVPS units are required. One unit AU-40N1.5-LCW(220V)(5m) provides the ionizer bias field, while four identical units float on an isolation transformer to supply:

1. The high-current heater for the ionizer (TB35V72A720W-Lgob)
2. The heater for the cesium reservoir (TB35V36A360W-Lgob)
3. The heater for the cesium transport line (TB35V36A360W-Lgob)
4. The sample target bias, which operates at –40 kV, using an AU-15N2-LCW(220V)(5m)

One additional HVPS AU-30N1-LC(220V)(5m) provides the negative bias for the Einzel lens, and four AP-1P(A) supplies independently drive each rod of the octupole deflector for X–Y beam steering. Figure 4.18 shows the digital HVPS control diagram, in which all power supplies are connected via fiber-optic links to a CO-HV interface adapter for isolated computer control and monitoring, and to a CO-E32 interface adapter for simultaneous control of multiple units without electrical noise.

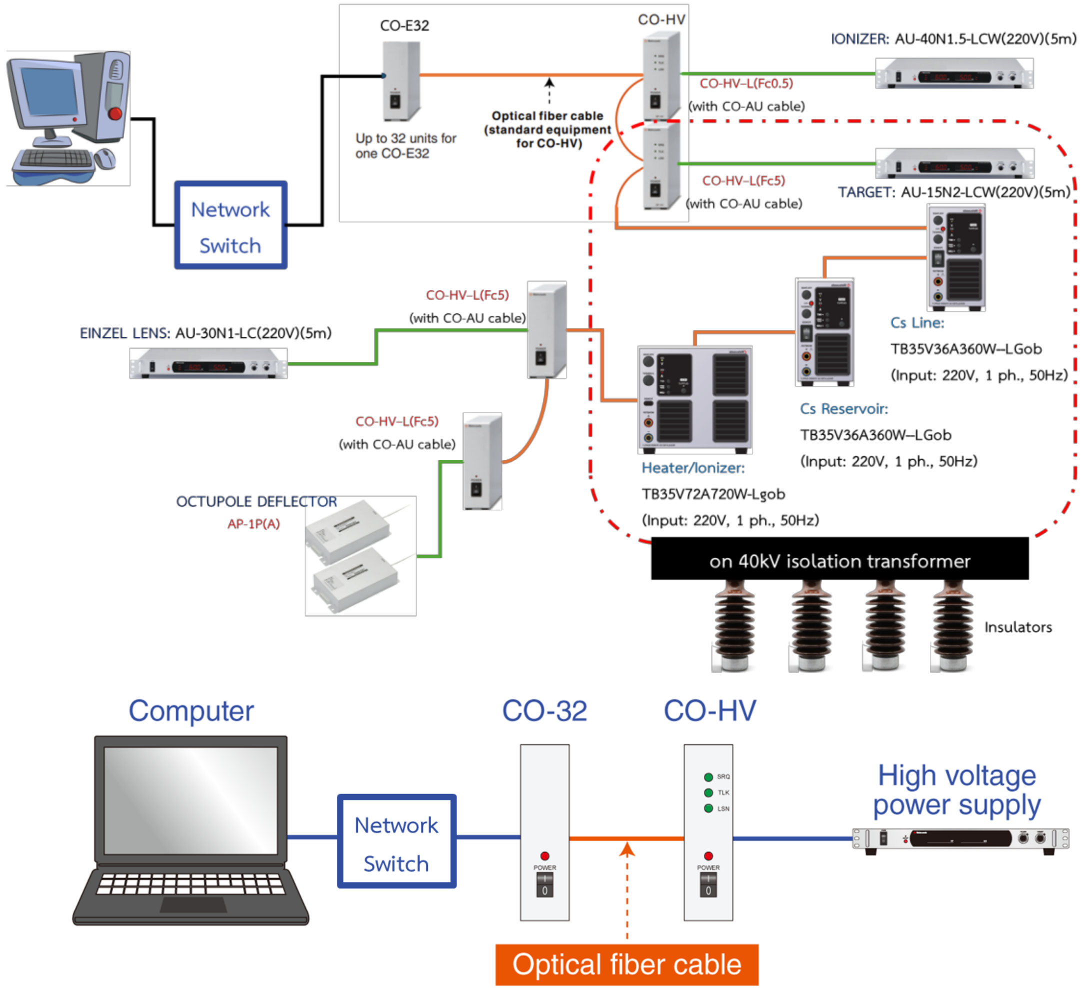

Figure 4.18 Diagram of the HVPS configuration used in the negative carbon ion beamline.

4.2.3 Integrated system

After confirming that all vacuum components were ready for use, collaboration with engineers from NARIT was undertaken to create 3D models in SolidWorks based on the measured dimensions of each chamber, some of which followed standard sizes. The chambers were then arranged in series, with appropriate ports and locations assigned. The beamline is designed to operate under ultra-high vacuum conditions (10^{-6} to 10^{-9} Torr) to minimize ion collisions with residual gas molecules. A gate valve is included to isolate the low-energy negative carbon ion beamline from the downstream bending magnet and acceleration section of the AMS system. Vacuum is maintained by turbomolecular pumps with pumping speeds of 300 L/s, 350 L/s, and 700 L/s, backed by a scroll pump, as shown in Figure 4.19.

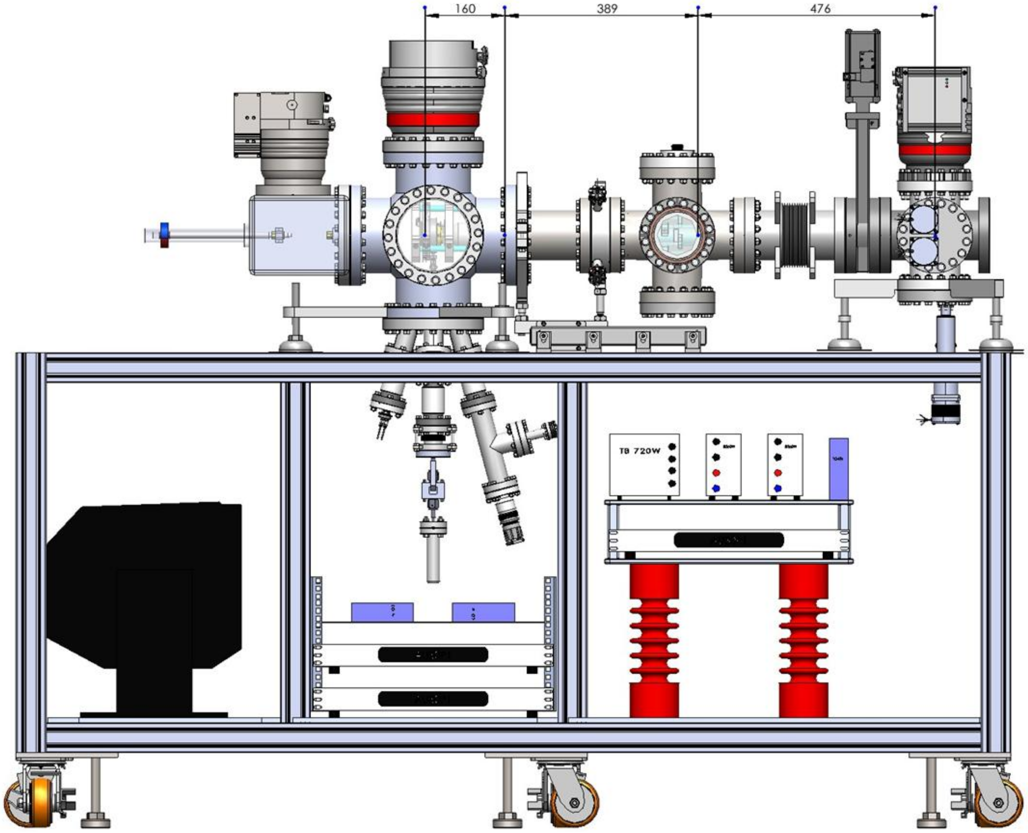

Figure 4.19 A compact system design for the low-energy negative carbon ion beamline, comprising a tabletop vacuum system integrated with HVPS units beneath the table. The ceramic insulator standoffs are shown in red, and the isolation transformer is shown in black.

High-voltage feedthroughs for the Einzel lens and octupole deflector, along with the pressure gauge and viewport, are installed on top of the tabletop vacuum chamber. The 160 mm distance shown in Figure 4.19 is measured from the sample target to the ion source's first focal point. The 389 mm distance extends to the center of the Einzel lens, and 476 mm reaches the aperture slit. This gives the electrostatic Einzel lens a magnification ratio of 476 mm / 389 mm ≈ 1.22, which is as close to 1 : 1 as practical within the constraints of the vacuum chamber and mounting supports.

The ion source's power supplies and high-voltage feedthroughs are integrated beneath the table. They include an isolation transformer (black) that powers each supply according to the diagram in Figure 4.18. All components rest on ceramic insulator standoffs (red), ensuring that the exterior of the vacuum chamber remains at ground potential for maximum safety.

4.3 The development of heater for ionizer

A tamper tool was 3D-printed at SUT QLAB to press alumina paste (Al_2O_3) into the grooves of the ionizer body, as shown in Figure 4.20. The tool was tested using green modeling clay as a stand-in for the alumina paste. The tamper successfully produced a layer approximately 1 mm thick; however, the surface exhibited ridges due to the layer lines from the 3D-printing process. For improved smoothness and durability, the tamper could be machined from aluminum using a lathe.

Figure 4.20 Pressing the tamper into modeling clay in the ionizer body's grooves, simulating the application of alumina paste (Al_2O_3).

In the filament heating tests shown in Figure 4.21, the pyrometer's measurement range was limited to a minimum of 249.0 °C and a maximum of 1370.1 °C. During the experiments, the supply current (I) and voltage (V) from the power supply were recorded, along with the pressure readings in both the test chamber and the pump, as summarized in Table 4.2. The filament was observed to first glow red at approximately 800 °C. After completing the heating cycle, the system was allowed to cool gradually before the vacuum pump was shut off, preventing air from entering the chamber and oxidizing the filament. This procedure helps extend the filament's operational lifetime.

Table 4.2 Recording data on MoRe filament heating under vacuum conditions. * Pressure was measured only during the first trial to study outgassing behavior at various temperatures.

Temp. (°C)	Volt (V)				Current (A)				Pressure @Chamber (Torr)	Pressure @Pump (Torr)
	1	2	3	Mean	1	2	3	Mean		
249.0	0.7	0.6	0.5	0.6	2.2	2.5	1.9	2.2	3.00E-04	4.70E-06
300.0	-	0.6	0.5	0.6	3.9	2.5	1.9	2.8	3.00E-04	4.70E-06
400.0	-	0.8	0.7	0.8	3.9	2.9	2.5	3.1	4.10E-04	6.20E-06
500.0	1.0	1.0	0.9	1.0	3.9	3.5	3.3	3.6	3.00E-04	4.90E-06
600.0	1.3	1.3	1.3	1.3	4.3	4.2	4.1	4.2	1.44E-04	3.00E-06
700.0	1.8	1.7	1.6	1.7	5.5	5.1	4.8	5.1	1.87E-04	3.30E-06
800.0	2.1	2.1	2.0	2.1	6.2	6.1	5.8	6.0	1.80E-04	3.50E-06
900.0	2.5	2.7	2.5	2.6	6.9	7.1	6.8	6.9	1.17E-04	2.50E-06
1000.0	3.0	3.3	3.0	3.1	7.8	8.3	7.8	8.0	1.21E-04	2.50E-06
1100.0	3.4	3.9	3.6	3.6	8.6	9.4	8.9	9.0	1.21E-04	2.60E-06
1200.0	4.0	4.7	4.2	4.3	9.7	10.8	10.0	10.2	1.29E-04	2.70E-06
1300.0	5.9	5.3	4.9	5.4	12.7	11.9	11.1	11.9	1.83E-04	3.30E-06
1370.1	6.2	5.8	5.4	5.8	13.3	12.7	12.0	12.7	1.83E-04	3.30E-06

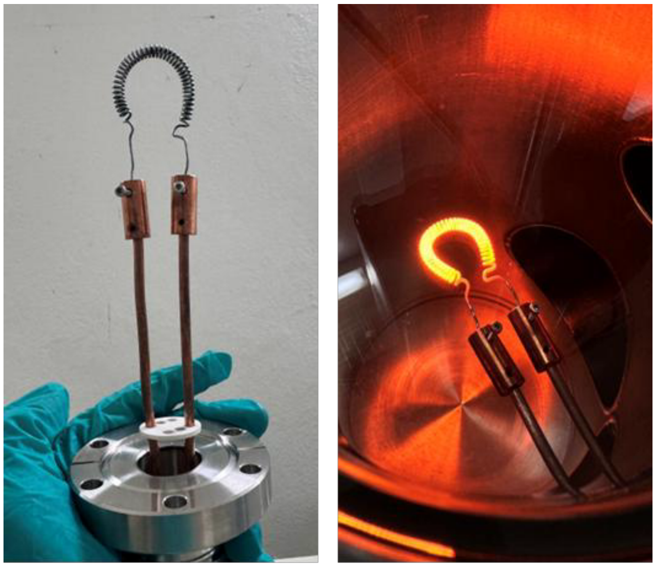

a) b)

Figure 4.21 MoRe heater coil a) Before installation b) During testing at 800 °C

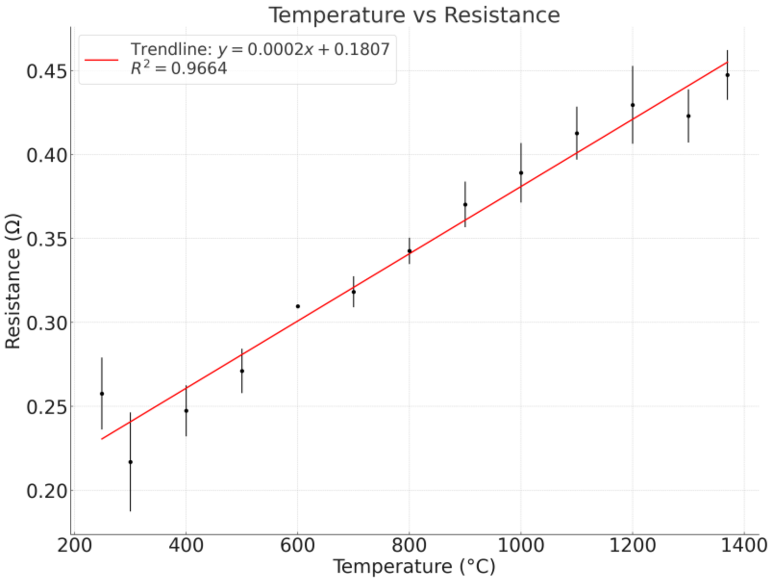

Figure 4.22 The graph shows the relationship between temperature and resistance.

The graph of Temperature vs Resistance in Figure 4.22 illustrates a typical behavior observed in metallic conductors. As the temperature increases, the resistance of the filament also increases. This positive correlation between temperature and resistance is due to the increased vibrations of the metal atoms at higher temperatures, which impedes the flow of electrons, thereby increasing resistance. The trendline in the graph is linear, confirming the material behaves according to the linear relationship described by the formula $R(T) = R_0[1 + \alpha(T - T_0)]$. The calculated R^2 value indicates that the linear model fits the data well, suggesting that the filament material's resistive properties follow expected behavior for most metals at these temperatures. The graph demonstrates a clear, predictable increase in resistance with temperature, which is crucial for applications where temperature control and resistivity are important, such as in heating elements and thermistors.

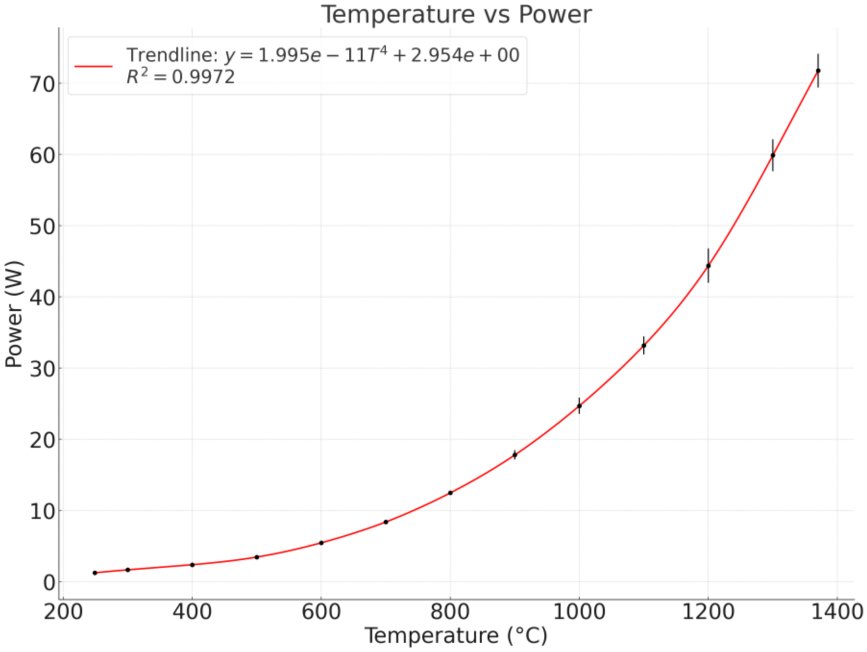

Figure 4.23 The graph shows the relationship between temperature and power consumption.

In the Temperature vs Power graph as shown in Figure 4.23, we observe the relationship between temperature and the power consumed by the filament. The power increases significantly as the temperature rises, following the relationship $P = IV$, where voltage and current increase with temperature. The trendline fits the data well using a T^4 model, which is consistent with the Stefan-Boltzmann law for radiation, suggesting that the energy radiated by the filament increases with the fourth power of its absolute temperature. The smooth curve shows a nonlinear increase in power with temperature, indicating that more energy is required to maintain the filament at higher temperatures. The R^2 value confirms a strong fit, showing that the power consumption behavior closely follows the theoretical model for radiative heat loss. This graph highlights the increasing demands on energy as the filament heats up, which is important for energy efficiency considerations in high-temperature applications.

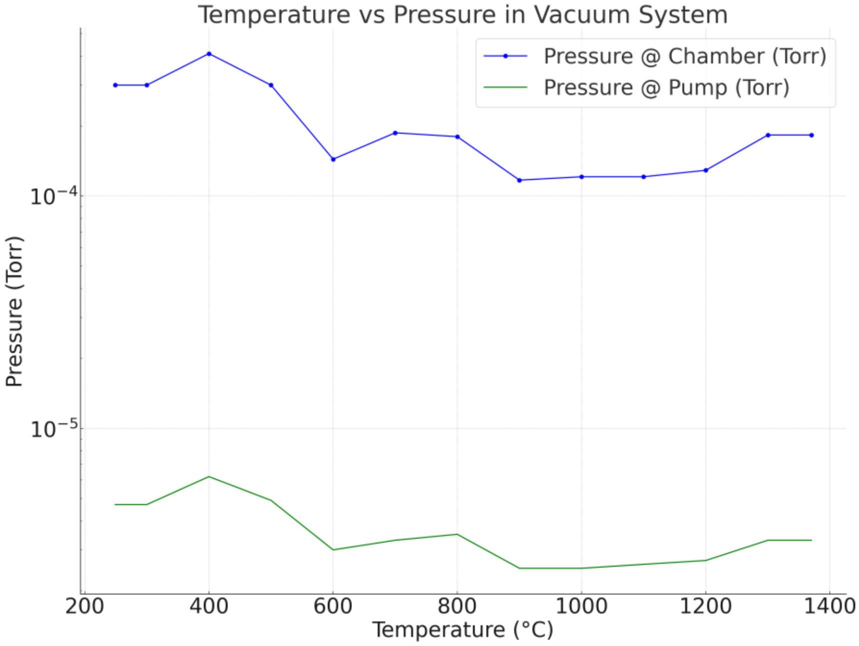

Figure 4.24 The graph shows the relationship between temperature and pressure in vacuum system.

The graph in Figure 4.24 presents the relationship between temperature and pressure at two locations within the vacuum system: the chamber and the pump. As temperature increases, pressure in both locations decreases, which is typical for vacuum systems. However, the chamber pressure remains consistently higher than the pump pressure, suggesting minor outgassing or leakage as the pump works to reduce the pressure further.

The data points follow a generally logarithmic decline with rising temperature. Using a logarithmic scale on the y-axis allows us to visualize small pressure changes at extremely low values, which would be difficult to discern on a linear scale. Interestingly, both pressures exhibit slight increases at approximately 400 °C, 800 °C, and 1300 °C, likely due to residual gases being released (outgassing) from chamber materials when heated.